

Role of plates and temperature-dependent viscosity in phase change dynamics

Shijie Zhong and Michael Gurnis¹

Department of Geological Sciences, University of Michigan, Ann Arbor

Abstract. The effects of plates and slabs on phase change dynamics have been investigated with convection models. Two complementary methods to simulate plates are used: material property and imposed surface velocity methods with temperature-dependent viscosity. For a wide range of model parameters, plates and slabs exert a significant control on phase change dynamics. As plate length (and hence plate age and convection cell aspect ratio) increases, both the propensity for slab penetration and the mass flux across an endothermic phase change increase. When cold downwellings are stiffened with a temperature-dependent rheology, slab penetration is enhanced, but total mass flux changes little. Plates organize large-scale flow and thermal structure and thereby affect phase change dynamics. As plates become larger, the resulting larger-scale structures are influenced less by endothermic phase changes, thus reducing the degree of layering. A model showing completely layered convection for a plate of unit length becomes unlayered when the plate is 3 or 5 times longer. For a given Clapeyron slope, the proportion of time for slab penetration increases from zero for cases with small plates to more than 0.5 for cases with large plates. The degree of layering, plate velocity, and mass flux are controlled by large-scale structures, while slab penetration may be more related to small-scale features. Therefore, whether or not subducted slabs penetrate the phase change may not necessarily indicate that convection is entirely layered or entirely unlayered. The episodicity of convection induced by an endothermic phase change strongly depends on plate length, rheology, and Clapeyron slope. A large plate and a stiff slab both weaken the episodicity of convection. Only for a certain range of Clapeyron slopes can the phase change induce a strong episodic thermal convection.

Introduction

Experimental petrology and the seismic velocity structure through the upper mantle suggest that the discontinuities at 410 km and 670 km probably result from solid-solid phase transitions from olivine to spinel and from spinel to a postspinel phase, respectively. The discontinuity at 670 km is of particular importance, since it would tend to retard mantle convection if it were endothermic [Schubert *et al.*, 1975]. Earlier studies have shown that the nature of an endothermic phase change at 670 km depth may determine if mantle convection is layered or if subducting slabs can penetrate into the lower mantle. With a two-dimensional, unit aspect ratio model, convection is layered and cold downwelling limbs are inhibited from penetrating into the lower layer, if the Clapeyron slope of the endothermic phase change is larger than $4\text{--}8 \text{ MPa K}^{-1}$ [Christensen and Yuen, 1984; 1985]. In models with a long box, multiple phase transitions, and depth-dependent thermal expansivity, the tendency for layered convection increases [Zhao *et al.*, 1992]. Recently, attention has focused on the time dependence induced by an endothermic phase change. In a spherically axisymmetric model, layered convection is intermittent, and strong downwellings

occasionally penetrate an endothermic phase boundary at 670 km depth [Machetel and Weber, 1991]. Intermittent layered convection has been found in various other models [Christensen and Yuen, 1985; Weinstein, 1993; Tackley *et al.*, 1993; Honda *et al.*, 1993]. In a three-dimensional spherical shell model, Tackley *et al.* [1993] reported that cold downwellings are temporarily stopped by the 670-km endothermic phase change but sink rapidly into the lower mantle.

The intermittence of layering reflects accumulation and release of negative buoyancy above the endothermic phase boundary [Machetel and Weber, 1991; Tackley *et al.*, 1993]. For cold downwellings, the endothermic phase boundary curves downward to generate a buoyancy retarding penetration. When penetration is retarded, cold material accumulates above the endothermic phase boundary. Simultaneously, hot upwellings are generally suppressed under the phase boundary. When this accumulated negative buoyancy dominates over that of the phase boundary deflection, the cold material penetrates into the lower layer; simultaneously, the hot upwelling fluid will be pushed into the upper layer. The exchange of mass between upper and lower layers can occur in short bursts (often described with superlatives such as "catastrophic" overturns, "avalanche" subduction, or "superplumes"). As the negative buoyancy is released, buoyancy associated with the deflection of phase boundary dominates and layering returns.

Whether convection is layered or not depends largely on whether the dominant buoyancy near the phase boundary is the negative thermal buoyancy or the positive phase change buoyancy. The negative thermal buoyancy results from the cooling of oceanic plates; the positive buoyancy depends on

¹Now at Seismological Laboratory, California Institute of Technology, Pasadena.

the Clapeyron slope and density jump associated with the phase change at 670 km depth, which can be constrained from experimental petrology and seismic velocity structure, respectively.

As oceanic plates move away from ridges, they cool and acquire a negative buoyancy, which is evident from the relation between lithospheric age, seafloor subsidence, and heat flow [Parsons and Sclater, 1977]. Oceanic plates continue to retain negative buoyancy along their way from oceanic ridges to oceanic trenches where they subduct into the mantle. With the temperature- and stress-dependent rheology of silicate rocks, oceanic plates are sufficiently strong such that they are rigid everywhere except at plate boundaries; the stiffness of oceanic plates gives plates two fundamental properties [Davies, 1988a]: (1) the horizontal dimension of oceanic plates can be much larger than the thickness of the mantle, e.g., Pacific plate is as long as 14,000 km; and (2) most of the negative buoyancy obtained while plates move away from oceanic ridges is retained within the plates, and the negative buoyancy will not be released until the plates subduct into the mantle. This suggests that the longer (or older) a plate is, the more negative buoyancy the plate has prior to subduction. It should be pointed out that the "flattening" of oceanic age-depth relation for seafloor older than 70 Ma [Parsons and Sclater, 1977] does not necessarily imply that plates do not cool after 70 Ma. The "flattening" can be attributed to the effects of hotspots [Heestand and Crough, 1981; Schroeder, 1984] and other dynamic processes under oceanic plates [Davies, 1988b, c; Cazenave and Lago, 1991; Davies and Pribac, 1993]. Recently, several studies on global seismic velocity structure also indicate that oceanic plates continue to cool after 70 Ma. Woodward and Masters [1991] reported that the differential *SS-S* and *PP-P* travel time residuals decrease almost linearly with square root of seafloor age to about 150 Ma; Su and Dziewonski [1992] reported similar results for *SS* residuals. The decrease in travel time residuals implies an increase in seismic velocities, which suggests a density increase or a temperature decrease. Zhang and Tanimoto [1991] showed that phase velocities of Love waves which primarily sample the shallow structure continuously increase with age of oceanic plates to 150 Ma.

While many numerical studies [e.g., Weinstein, 1993; Tackley et al., 1993] have used realistic mantle material properties including the Clapeyron slope and density jump of the 670-km phase change, oceanic plates are poorly simulated in all studies with constant viscosity. Constant viscosity inherently precludes the formation of long and rigid oceanic plates. For models with a Rayleigh number larger than 10^6 , a top thermal boundary layer quickly breaks down into small downwelling cold limbs, and the characteristic length between these top thermal boundary layers is usually comparable to the thickness of the mantle (see typical thermal structures of Peltier and Solheim [1992] and Machetel and Weber [1991]), which is thus considerably shorter than that of the Pacific plate. For those models with unit aspect ratio [e.g., Christensen and Yuen, 1985], the length of top thermal boundary layer is naturally smaller than the thickness of the box. As pointed out above, a shorter plate would give less negative buoyancy within the plate prior to subduction and hence less chance for the subducting slab to penetrate into the lower mantle. Moreover, it has been shown that plate-scale flow and thermal structures induced by the motion of rigid plates are the predominant structures within the mantle and are

essential to explaining surface observables including heat flux, seafloor subsidence, and geoid [Davies, 1988a, b, c]. Indeed, in any great circle profile of the Earth's mantle, there are no more than three subduction zones. However, in most previous isoviscous models with phase changes, thermal structure within the mantle is dominated by small-scale structure [e.g., Peltier and Solheim, 1992] which leads to great difficulties in explaining surface observables [Davies, 1988c]. Even in the three-dimensional spherical shell models of Tackley et al. [1993], although thermal structure is characterized by relatively large aspect ratio features, there are still on average more than six downwellings per great circle path. Models with large plates are essential if comparisons are made with observations, since most of our seismological understanding of the transition zone comes from the western Pacific where the oceanic lithosphere is old. Since phase changes may have less effects on large-scale thermal structure than on small-scale plume structures, the dominant large-scale flow and thermal structures may result in different phase change dynamics than do the small-scale structures from isoviscous convection models. Isoviscous models have also failed to incorporate slab strength. Subducted slabs are stiffer than ambient mantle due to their lower temperature; stiffer slabs have more capacity to retain their integrity and perhaps may have a greater ability to penetrate into the lower mantle [Christensen and Yuen, 1984]. It is clearly essential to study phase change dynamics in the presence of both long plates and stiff slabs.

Realistic plates and subducted slabs have been incorporated into two-dimensional Cartesian models with phase changes. A successful plate model must be capable of producing "plate-like" surface deformation; i.e., strain is concentrated at plate boundaries and is insignificant within the plate interior. For relatively small size plates, various methods including material properties [Gurnis and Hager, 1988; King and Hager, 1990], force balance [Gable et al., 1991], and power-law thin sheets [Weinstein and Olson, 1992] have been used [King et al., 1992]. For large size plates, Davies [1988a] used imposed surface velocity with temperature-dependent viscosity. In the material property method, the oceanic plates are simulated by imposing high viscosity for the top boundary layer and two weak margins on the periphery; the length of plates can be varied by changing the aspect ratio of the box. Although the material property method is an effective method to simulate plates, it cannot easily account for stiff slabs. An imposed surface velocity method with temperature-dependent viscosity can simulate both plates and stiff slabs, but it is computationally costly. In this study, both the material property method and the imposed surface velocity method with temperature-dependent viscosity are used to investigate different effects of plates and stiff slabs on phase change dynamics.

Our computations for a wide range of parameters show that plates and stiff slabs significantly affect phase change dynamics. As plate length increases, mass flux across the endothermic phase change increases, degree of layering decreases, and slab penetration occurs more frequently. Stiff slabs enhance slab penetration substantially but have little effects on global features including the total mass flux and degree of layering. Finally, large size plates can be well simulated using material property methods, even in the presence of both endothermic and exothermic phase changes.

Physical Models and Method

Equations and Model Setup

The governing equations for mantle convection are derived from the conservation of mass, momentum and energy. Because the mantle has a very high Prandtl number, the inertial terms in the momentum equation are negligible. With the Boussinesq approximation, the fluid is effectively incompressible [McKenzie *et al.*, 1974]. The momentum, continuity, and energy equations are, respectively,

$$\sigma_{ij,j} + f_i = 0, \quad (1)$$

$$u_{i,i} = 0, \quad (2)$$

$$\frac{\partial T}{\partial t} + u_i \cdot T_{,i} = \kappa T_{,ii} + H, \quad (3)$$

where u_i , f_i , and σ_{ij} are the flow velocity, the body force, and the stress tensor, respectively; T is the temperature; t is the time; κ is the thermal diffusivity; H is the heat source; and i and j are spatial indices. Throughout the paper, $A_{,i}$ represents partial derivative of function A with respect to coordinate x_i ; repeated spatial indices denote summation. The body force vector and the stress tensor may be expressed in terms of an equation of state and a constitutive equation as

$$f_i = -\rho_0[1 - \alpha(T - T_0) + \sum_k \Gamma_k \frac{\Delta \rho_k}{\rho_0}]g\delta_{i2}, \quad (4)$$

and

$$\sigma_{ij} = -P\delta_{ij} + \mu(u_{i,j} + u_{j,i}), \quad (5)$$

where ρ_0 and T_0 are the reference density and temperature, respectively; g is the gravitational acceleration; α is the coefficient of thermal expansion; k is the index for phase change; Γ_k and $\Delta \rho_k$ are the dimensionless phase change function and density jump for the k th phase change, respectively; P is the pressure; and μ is the dynamic viscosity.

Equations (4) and (5) are substituted into equations (1), (2), and (3), and nondimensionalized by introducing the following characteristic scales (where the primed variables are dimensionless):

$$x_i = Dx'_i; \quad u_i = U_0 u'_i; \quad T = (T_b - T_0)\theta + T_0; \quad t = t' D/U_0; \\ E = \frac{HD^2}{\kappa(T_b - T_0)}; \quad P = \frac{\mu_r U_0}{D} P'; \quad U_0 = \kappa/D; \quad (6)$$

where T_b and T_0 are the temperatures on the bottom and top boundaries, respectively; D is the thickness of the box; θ is the nondimensional temperature; μ_r is a reference dynamic viscosity, which is chosen as the viscosity appropriate for the temperature on the bottom boundary for cases with temperature-dependent viscosity and otherwise is chosen as the background viscosity. The model and material parameters are listed in Table 1. The nondimensional equations are (primes have been dropped for simplicity)

$$\sigma_{ij,j} + (R_a \theta - \sum_k R_b^k \Gamma_k) \delta_{i2} = 0; \quad (7)$$

$$u_{i,i} = 0; \quad (8)$$

Table 1. Physical and Geometrical Model Parameters

Parameter	Value
Thickness of the box D	1.5×10^6 m
Thickness of the lithosphere	1.0×10^5 m
Temperature contrast $T_b - T_0$	2000 K
Reference density ρ_0	3.3×10^3 kgm ⁻³
Thermal diffusivity κ	10^{-6} m ² s ⁻¹
Acceleration of gravity g	10 m s ⁻²
Thermal expansion α	2.0×10^{-5} K ⁻¹
Thermal Rayleigh number R_a	10^6
Equilibrium depth for the exothermic phase change	4.1×10^5 m
Equilibrium depth for the endothermic phase change	6.7×10^5 m
Equilibrium temperature for the exothermic phase change	1200 K
Equilibrium temperature for the endothermic phase change	
Bottom heating	1000 K
Internal heating	1400 K
Density jumps across the phase change boundaries	8%
Phase transition widths d	3.75×10^4 m

$$\frac{\partial \theta}{\partial t} + u_i \cdot \theta_{,i} = \theta_{,ii} + E; \quad (9)$$

where in equation (7), the hydrostatic pressure has been eliminated; R_a and R_b^k are the thermal Rayleigh number and phase change Rayleigh number for the k th phase change, respectively. Their definitions are

$$R_a = \frac{\rho_0 g \alpha (T_b - T_0) D^3}{\kappa \mu_r}; \quad (10)$$

$$R_b^k = \frac{\Delta \rho_k g D^3}{\kappa \mu_r}; \quad (11)$$

The approach to incorporate phase changes is similar to that of Richter [1973] and Christensen and Yuen [1985]. We define an "excess pressure" as

$$\pi_k = P - P_0 - \gamma_k T, \quad (12)$$

where γ_k and P_0 are the Clapeyron slope and phase change pressure at zero degree temperature for the k th phase change. After nondimensionalizing pressure terms and γ_k by $\rho_0 g D$ and $\rho_0 g D / (T_b - T_0)$, respectively, and ignoring the nonhydrostatic pressure, the nondimensional "excess pressure" can be written as

$$\pi_k = 1 - d_{rk} - x_2 - \gamma_k (\theta - \theta_{rk}), \quad (13)$$

where γ_k , d_{rk} , and θ_{rk} are the nondimensional Clapeyron slope, reference phase transition depth, and reference phase transition temperature for the k th phase change, respectively. For the 410-km and 670-km phase changes, d_{rk} are 0.273333 and 0.446667, respectively. θ_{rk} vary from case to case depending on heating modes; θ_{rk} are 0.5 for noninternal heating cases, and for internal heating cases, θ_{rk} are 0.6 and 0.7 for the 410-km and 670-km phase changes, respectively. The dimensionless phase change function for the k th phase change, Γ_k , is then defined as

$$\Gamma_k = \frac{1}{2} (1 + \tanh \frac{\pi_k}{d}), \quad (14)$$

where d , the dimensionless phase transition width, is 0.025 (which scales to 37.5 km) for all the phase changes in this study.

Plates are simulated either through the material property method or an imposed surface velocity. For the material property method, a 100-km-thick layer near the surface is assigned a viscosity 10^3 times the interior viscosity, and this region represents a plate (Figure 1). Two margins of the plate have a viscosity 0.1 time the interior viscosity (Figure 1). The low viscosity for the two margins and the high viscosity for the plate are designed to mimic a stress- and temperature-dependent rheology. Plates with different length can be obtained by varying the aspect ratio of the box. To use temperature- and stress-dependent rheology is computationally costly, since the stiffness matrix would need to be factorized numerous times for each time step. However, for the material property method, the factorization of the stiffness matrix is only needed once at the beginning of each calculation; therefore the material property method is an efficient and effective method for modeling plates, and we will use this method to mainly study effects of plates on phase change dynamics.

Temperature-dependent viscosity is necessary to investigate the effects of stiff subducted slabs. While temperature-dependent viscosity gives rise to both stiff plates and slabs, it causes plates to become immobile [e.g., Gurnis, 1989]. Therefore imposing a constant surface velocity is necessary to have a realistic plate [Davies, 1988a]. By imposing a constant surface velocity in temperature-dependent viscosity models, plates and stiff slabs can be well simulated. We have found that the imposed surface velocity method does not alter the dynamics, as long as the imposed surface velocity is equal to the average plate velocity determined from the material property method. The temperature dependence of viscosity is defined as

$$\mu = \exp\left(\frac{c_1}{\theta + c_2} - \frac{c_1}{1 + c_2}\right), \quad (15)$$

where constants c_1 and c_2 determine both the range of viscosity variations within the fluid and the viscosity drop across top thermal boundary layer. In this study, two sets of constants c_1 and c_2 have been used. Both sets of constants limit the viscosity to vary from 1 to 10^3 as nondimensional temperature changes from 1 to 0, but the viscosity drops across the top thermal boundary layer are different (Figure 2).

Isothermal boundary conditions are applied on the top and bottom boundaries; reflecting boundary conditions are used for

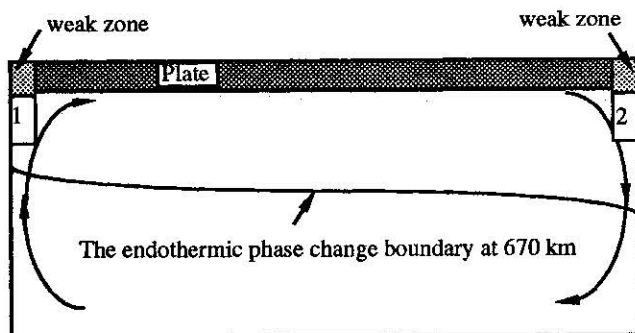


Figure 1. Model setup using the material property method. The numbers represent regions in which mean temperatures are measured. Regions 1 and 2 overlap the weak zones.

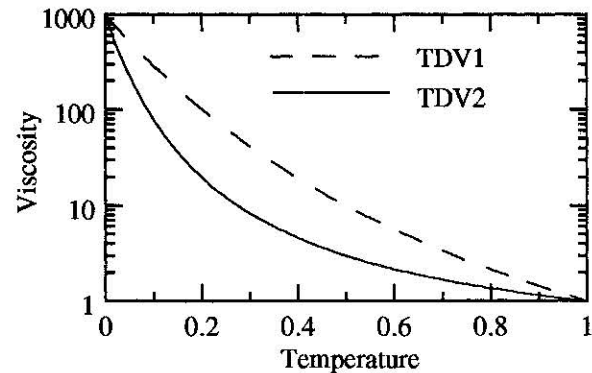


Figure 2. The temperature dependence of viscosity. For TDV1, c_1 and c_2 are 13.82 and 1.0, respectively; for TDV2, c_1 and c_2 are 1.987 and 0.2332, respectively.

the side walls; and free slip boundary conditions are applied on the top and bottom boundaries except for the cases with imposed surface velocity. The initial conditions depend on the aspect ratio. For a given aspect ratio, a case with no phase change is run with an initial condition,

$$\theta(x_1, x_2) = 1 - x_2 + \epsilon \cos\left(\pi \frac{x_1}{L}\right) \sin(\pi x_2), \quad (16)$$

to check whether a "plate-like" surface deformation can be obtained using the material property method, where in equation (16), ϵ , the perturbation, is 0.01; L is the aspect ratio or the plate length. For all the cases with phase changes, the initial conditions are taken from the last frame of that run with no phase changes for the corresponding aspect ratio.

The equations are solved with a finite element code: ConMan [King *et al.*, 1990]. A penalty formulation is used to solve the momentum equation and to enforce incompressibility [Hughes, 1987]. The energy equation is solved with a streamline upwind Petrov-Galerkin method [Brooks, 1981]. There are 80 elements in the vertical direction and 80 to 250 elements in the horizontal direction, depending on the aspect ratio of the box. By refining meshes, sufficient resolution is acquired in plates, plumes, and phase transition zones. There are more than seven elements to resolve the top and bottom thermal boundaries and the upwelling and downwelling limbs near the side walls. We have compared results from our ConMan code with phase changes with results from a finite difference code discussed by Weinstein [1993]; Nusselt numbers for test cases agree well between the codes with differences of less than 1%.

It should be pointed out that due to computational limitations our models are simplified in both material property and geometry, compared to Earth's mantle. The three-dimensional spherical geometry of Earth may give rise to different forms of upwellings and downwellings from those observed in two-dimensional models, which may affect the ability of mass exchange across the phase change boundary [Tackley *et al.*, 1993]. The thickness of the box in our models is only half the depth of the mantle; the small thickness of the box may reduce the potential of thermal buoyancy and thus affects the phase change dynamics. A more realistic rheology of Earth's mantle may result in a larger viscosity contrast than 10^3 in our models, and the larger viscosity contrast would give rise to stiffer plates and slabs than those in our models. However, we think that the effects of tectonic plates and stiff subducted slabs on phase change dynamics, which are

demonstrated in our models, are essential for understanding the thermal and chemical structure of Earth's mantle.

Measures of Temporal and Spatial Dependencies

Several measures are made to study the dynamics of slab penetration and the layering of convection. First, a slab penetration velocity V_s is defined as

$$V_s = \frac{1}{\Delta x} \int_{L-\Delta x}^L u_2^{endo}(x_1) dx_1, \quad (17)$$

where Δx is 0.0667 (or 100 km) and u_2^{endo} is the vertical velocity on the 670-km endothermic phase change boundary. With the initial conditions used, a strong downwelling limb (subducting slab) is assured on the right side of the box (Figure 1). Second, a mass flux through the entire endothermic phase change boundary is defined as

$$M_v = \int_{\Gamma_{endo}} u_n^{endo}(t) dl, \quad (18)$$

where the line integral is taken along the endothermic phase change boundary, Γ_{endo} , and u_n^{endo} is the normal velocity on Γ_{endo} . A maximum horizontal mass flux is defined as

$$M_h = \max_{0 \leq x_1 \leq L} \int_0^1 u_1(x_2) dx_2, \quad (19)$$

Since M_v should be zero for perfect layered convection but close to M_h for a convection cell which completely penetrates the phase change, the ratio of M_v to M_h measures the degree of layering. Third, a parameter R_s is defined as the fraction during which slab penetration velocity V_s is more than 80% of plate velocity U_p , where U_p is the average surface velocity. Fourth, average temperatures in upwelling, T_u , and downwelling, T_d , are computed (see Figure 1 for the regions in which the averages are computed). The differential temperature, $T_u - T_d$, is a measure of the largest-scale thermal buoyancy.

Besides these four measures, we also compute mean temperature T_m , surface heat flux F , internal heating rate ξ , plate velocity U_p , and plateness P . The procedures to calculate surface heat flux and internal heating rate are identical to those given by Zhong and Gurnis [1993]. Following Weinstein and Olson [1992], plateness measures how well a model plate achieves "plate-like" behavior:

$$P = \frac{1}{\pi - 2} \left(\pi - \frac{1}{U_p} \int_0^L \left| \frac{du_1(x_1, 1)}{dx_1} \right| dx_1 \right), \quad (20)$$

where $u_1(x_1, 1)$ is the surface horizontal velocity. P is a number between 0 and 1; P is 1 when the surface velocity becomes a box-car function (i.e., a plate) and 0 for a sinusoidal function surface velocity. However, caution must be exercised in using this characterization because minor kinks in the surface horizontal velocity profile, which may be visually insignificant, can significantly reduce P .

Results and Discussions

Plates affect phase change dynamics in two ways. First, by inducing a predominantly plate-scale flow, plates control the large-scale buoyancy distribution and thus affect the mass exchange across the endothermic phase change boundary.

Second, by retaining the negative buoyancy of a cooling thermal boundary layer, plates of different sizes control the amount of negative buoyancy prior to the intersection of the phase boundary. Subducted slabs are stiffer than ambient mantle, due to the lower temperature of slabs, and stiff slabs tend to retain their integrity and thus have a larger chance to penetrate into the lower mantle. These effects of plates and stiff subducted slabs on phase change dynamics are evident in our numerical models for a wide range of parameters. In what follows, we will first present calculations incorporating plates of large size relative to the box depth using the material property method; second, we show the effects of plates on endothermic phase change dynamics and on multiple phase change dynamics; finally, we study the effects of stiff slabs on slab penetration using temperature-dependent viscosity.

Simulation of Plates Through the Material Property Method

Plates are simulated with a material property method. With the material property method, the surface velocity of plates with a length comparable to the box height has been shown to be "plate-like" [Gurnis, 1989; King *et al.*, 1992]; however, no similar results have yet been reported for large size plates.

Models with plates whose lengths are 1, 2, 3 and 5 times the box height (cases 1, 2, 3, and 4, respectively in Table 2) show that the material property method can yield a "plate-like" surface velocity for plates with P greater than 0.9 (Table 2). These cases have no phase change and are heated entirely from below (Table 2) with $R_a = 10^6$ (R_a is 10^6 for all the cases in this study unless otherwise specified). Plate-scale flow and thermal structure predominate and "plate-like" behavior is well simulated even for an L of 5 (representative surface velocity profiles, temperature fields and stream functions for cases with $L = 1, 3$, and 5 are shown in Figure 3). Plates continue to cool until they reach the weak margins where the cold fluid plunges into the fluid interior.

As L increases, we observe that time-averaged vertical and horizontal mass flux $\langle M_v \rangle$ and $\langle M_h \rangle$, plate velocity $\langle U_p \rangle$, and slab penetration velocity $\langle V_s \rangle$ in general increase (Table 2). The amount of increase is less than 50%, as L increases from 1 to 5 (Table 2). The ratios of $\langle M_v \rangle$ to $\langle M_h \rangle$ are all slightly larger than 1 with a maximum of 1.25 for case 2 (Table 2), and this has two implications: (1) a single-cell flow organized by the plate predominates, independent of plate length; (2) the ratio of $\langle M_v \rangle$ to $\langle M_h \rangle$ should be close to 1 for unlayered convection with plates. We also observe that as L increases, the time-averaged heat flux F through the surface decreases, but the mean temperature T_m and the temperature difference between upwelling and downwelling $\langle \delta T_h \rangle$ (i.e., $T_u - T_d$) generally increase (Table 2). When significant internal heating is included (cases 5, 6, 7, and 8 for $L = 1, 2, 3$, and 5, respectively, in Table 2), plate-scale flow predominates, and plates are well-simulated (Table 2), similar to the no internal heating cases. However, $\langle M_v \rangle$, $\langle M_h \rangle$, and $\langle U_p \rangle$ are significantly smaller than those for no internal heating cases for $L = 1, 2$, and 3.

The plate-scale flow structures (e.g., Figures 3b and 3c) are similar to those with prescribed surface velocity and temperature-dependent viscosity [Davies, 1988a] but are significantly different from models with no plates in which flow structures are of much smaller wavelength (e.g., Figure 4a shows representative temperature and flow fields for case 9 with isoviscous flow (Table 2); case 9 is identical to case 3

Table 2. Model Parameters and Statistics of Models

Case	Mode	L	E	γ_1	γ_2	R_s	$\langle M_v \rangle$	$\langle M_h \rangle$	$\langle V_s \rangle$	$\langle U_p \rangle$	$\langle \delta T_h \rangle$	P	F	$\xi_s\%$	T_m
1	MP	1	0	—	—	1.0	545(9)	545(11)	1450(16)	697(5)	0.30	0.91	20.0	0	0.52
2	MP	2	0	—	—	1.0	619(40)	494(39)	1665(89)	703(55)	0.42	0.95	14.8	0	0.54
3	MP	3	0	—	—	1.0	682(63)	572(44)	1928(126)	710(71)	0.41	0.95	12.3	0	0.59
4	MP	5	0	—	—	1.0	776(73)	659(60)	2167(177)	790(77)	0.45	0.93	10.2	0	0.61
5	MP	1	8	—	—	1.0	398(51)	394(58)	1451(72)	562(47)	0.31	0.91	19.5	24	0.61
6	MP	2	8	—	—	1.0	493(41)	474(39)	1757(107)	614(74)	0.42	0.94	15.2	26	0.64
7	MP	3	8	—	—	1.0	575(51)	536(49)	1964(129)	622(70)	0.42	0.93	13.1	26	0.68
8	MP	5	8	—	—	1.0	773(28)	704(28)	2396(88)	782(30)	0.48	0.92	11.6	23	0.70
9	CV	—	0	—	—	—	1331(412)	693(199)	—	528(256)	—	—	17.3	0	0.50
10	CV	—	0	—	-0.17	—	101(32)	301(30)	—	340(54)	—	—	9.5	0	0.52
11	MP	1	0	—	-0.17	0.05	34(18)	212(30)	113(85)	300(44)	0.33	0.90	10.5	0	0.54
12	MP	2	0	—	-0.17	0.38	212(210)	288(196)	350(414)	398(220)	0.42	0.81	11.2	0	0.60
13	MP	3	0	—	-0.17	0.48	333(144)	395(169)	502(502)	466(174)	0.47	0.92	10.2	0	0.62
14	MP	5	0	—	-0.17	0.48	465(120)	471(120)	518(445)	541(124)	0.56	0.94	9.01	0	0.64
15	MP	1	8	—	-0.17	0.00	26(2)	188(6)	100(11)	325(4)	0.33	0.89	12.7	55	0.66
16	MP	2	8	—	-0.17	0.32	195(172)	270(157)	319(411)	426(182)	0.49	0.84	14.4	42	0.72
17	MP	3	8	—	-0.17	0.43	284(118)	329(137)	461(482)	469(146)	0.52	0.92	12.7	41	0.76
18	MP	5	8	—	-0.17	0.48	410(123)	423(150)	532(534)	516(129)	0.57	0.92	10.9	43	0.79
19	MP	1	8	—	-0.19	0.01	21(8)	183(28)	75(43)	316(5)	0.31	0.91	11.5	61	0.66
20	MP	2	8	—	-0.19	0.00	47(24)	234(40)	8(3)	362(18)	0.52	0.92	11.0	65	0.70
21	MP	3	8	—	-0.19	0.30	239(134)	294(140)	319(434)	436(154)	0.54	0.90	12.6	43	0.76
22	MP	5	8	—	-0.19	0.33	333(92)	358(128)	333(480)	466(108)	0.61	0.91	10.8	48	0.79
23	MP	3	8	—	-0.12	1.0	379(66)	369(46)	965(129)	564(90)	0.45	0.93	13.0	33	0.72
24	MP	3	8	—	-0.15	0.51	321(130)	355(146)	564(484)	494(155)	0.48	0.91	12.8	37	0.76
25	MP	3	8	—	-0.21	0	96(36)	265(60)	149	396(37)	0.65	0.93	12.1	56	0.73
26	MP	1	8	0.17	-0.17	0.19	133(195)	243(166)	276(383)	431(249)	0.25	0.80	17.5	32	0.61
27	MP	2	8	0.17	-0.17	0.31	286(257)	342(230)	451(581)	505(331)	0.35	0.81	14.3	29	0.68
28	MP	3	8	0.17	-0.17	0.43	409(198)	426(180)	567(599)	616(252)	0.39	0.90	13.3	32	0.70
29	MP	5	8	0.17	-0.17	0.54	541(171)	508(143)	697(612)	683(171)	0.43	0.90	11.4	29	0.72
30	TDV1	—	8	—	-0.17	—	47(10)	170(26)	—	74(4)	—	—	8.71	88	0.85
31	MPI	3	8	—	—	1.0	560(29)	522(13)	1925(53)	622	0.52	1.0	13.0	30	0.68
32	MPI	3	8	—	-0.17	0.42	294(60)	334(105)	458(440)	469	0.60	1.0	12.5	39	0.76
33	TDV1	3	8	—	—	1.0	409(48)	374(20)	948(22)	622	0.67	1.0	14.1	40	0.77
34	TDV1	3	8	—	-0.17	0.99	228(45)	244(35)	444(17)	469	0.74	1.0	13.5	49	0.84
35	TDV1	3	8	—	-0.21	0.26	93(7)	197(9)	313(13)	396	0.81	1.0	13.1	57	0.83
36	TDV2	3	8	—	-0.17	0.59	263(57)	276(79)	417(192)	469	0.71	1.0	13.5	51	0.83

In the column of mode, MP, CV, MPI, TDV1, and TDV2 stand for material property plate, constant viscosity, material property with imposed surface velocity plate, temperature-dependent viscosity with TDV1 (Figure 2), and temperature-dependent viscosity with TDV2 (Figure 2), respectively; the numbers in parentheses are the standard deviations.

except the rheology). Since multicell convection (i.e., small-scale flow structure) characterizes the flow for the isoviscous flow case (case 9), the ratio of $\langle M_v \rangle$ to $\langle M_h \rangle$ for case 9 is about twice larger than that for case 3 in which a single-cell convection characterizes the flow (Table 2).

Endothermic Phase Change Dynamics With a Plate

Inclusion of an endothermic phase change at 670 km depth may lead to layered convection if the Clapeyron slope and density contrast across the phase change are sufficiently large [Christensen and Yuen, 1984; 1985]. The critical Clapeyron slope for layered convection may decrease with increasing Rayleigh number R_a [Christensen and Yuen, 1985; Zhao et al., 1992]. In this section, we shall focus on the effects which plates have on thermal convection with phase changes.

In order to better examine the effect of a plate on phase change dynamics, an isoviscous flow (case 10 in Table 2) with an endothermic phase change is computed; the inclusion of the phase change is the only difference between this case (case 10) and the previous isoviscous flow case (case 9) (Table 2). For

this entirely bottom heated case, the thermal Rayleigh number R_a , phase change Rayleigh number R_b , and nondimensional Clapeyron slope γ are 10^6 , 2×10^6 , and -0.17 (Table 2), respectively. In this study, R_b for either exothermic or endothermic phase changes is always twice that of R_a , i.e., 2×10^6 , unless otherwise specified. The density jump across the phase boundary and the Clapeyron slope, after scaling with the material parameters in Table 1, are 8% and -4.21 MPa K⁻¹, respectively. For this isoviscous case (case 10), the endothermic phase change results in clearly layered convection, which is evident through representative temperature and stream functions (Figure 4b) and a ratio of $\langle M_v \rangle$ to $\langle M_h \rangle$ which is only about 0.3 (Table 2). Since an endothermic phase change retards convection, $\langle M_v \rangle$ and $\langle M_h \rangle$ are much smaller, compared with those without the phase change (Table 2). It should be pointed out that for the R_a , Clapeyron slope, and density jump used in case 10, thermal convection was also reported to be predominantly layered in an isoviscous flow model in a unit aspect ratio box [Christensen and Yuen, 1985].

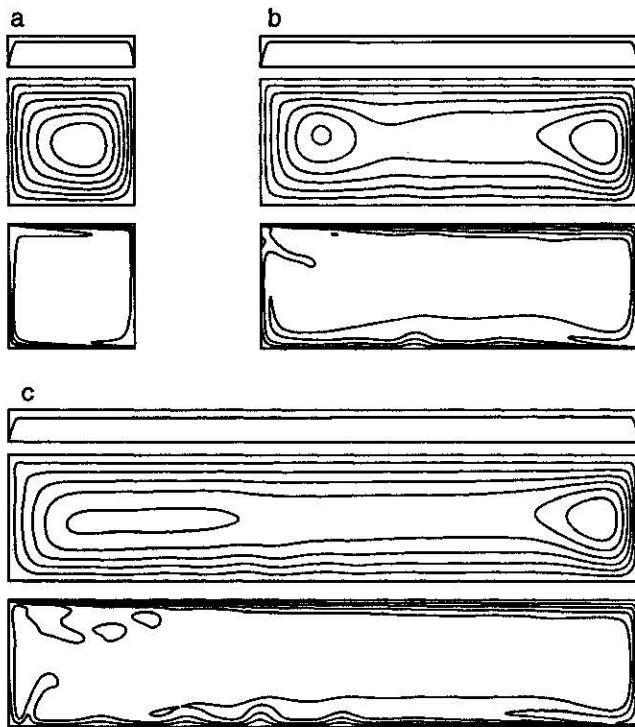


Figure 3. Representative temperature and stream functions for (a) case 1 with $L = 1$, (b) case 3 with $L = 3$, and (c) case 4 with $L = 5$. In each part, the top panel is surface velocity, the middle panel is the stream function, and the bottom panel is the temperature. All three temperature fields have the same contours.

Models with the same R_a , R_b , γ , and internal heating parameter E as those in case 10 but with a plate (cases 11, 12, 13, and 14 in Table 2 for $L = 1, 2, 3$, and 5 , respectively) show that plates exert a fundamental control on phase change dynamics. For $L = 1$, the flow structures are characterized by two layered convection (Figure 5a) and differs significantly from those excluding any phase change (Figure 3a), indicating an important role of phase change in determining the thermal structure for $L = 1$. The layered flow structures are similar to those of *Christensen and Yuen* [1985], suggesting that small plates do not significantly change the results of isoviscous flows. However, flows for models with long plates are characterized by plate-scale structure (Figures 5b and 5c for representative temperature and flow fields for cases 13 and 14 with $L = 3$ and 5 , respectively). These plate-scale thermal structures for long plates (Figures 5b and 5c) are very similar to those in flows including plates and lacking a phase change (e.g., Figures 3b and 3c), but differ significantly from those in flows including a phase change and lacking plates (e.g., Figure 4b for case 10). This suggests that for $L = 3$ and 5 , flow structures are primarily determined by the scale of plates not the phase change. The endothermic phase change has much larger effects on flow structures for models with small plates than for models of large plates, and for a large plate, the flow structures are predominantly controlled by the scales of the plate.

The phase change introduces an episodic time dependence. The effects of a phase change on the temporal evolution of mass flux M_v across the phase boundary, slab penetration velocity V_s , and plate velocity U_p also strongly depend on

plate length. For $L = 1$, convection is predominately layered, evident from the layered flow structures (Figure 5a). V_s is always significantly smaller than plate velocity U_p at any given time (Figure 6a), indicating insignificant slab penetration; M_v is also considerably smaller than M_h , indicating layered convection and no significant mass exchange across the phase change boundary. For L greater than 2 , M_v becomes nearly as large as M_h ; V_s is frequently much larger than plate velocity (Figures 6b and 6c for cases 13 and 14 with $L = 3$ and 5 , respectively), showing a diminished

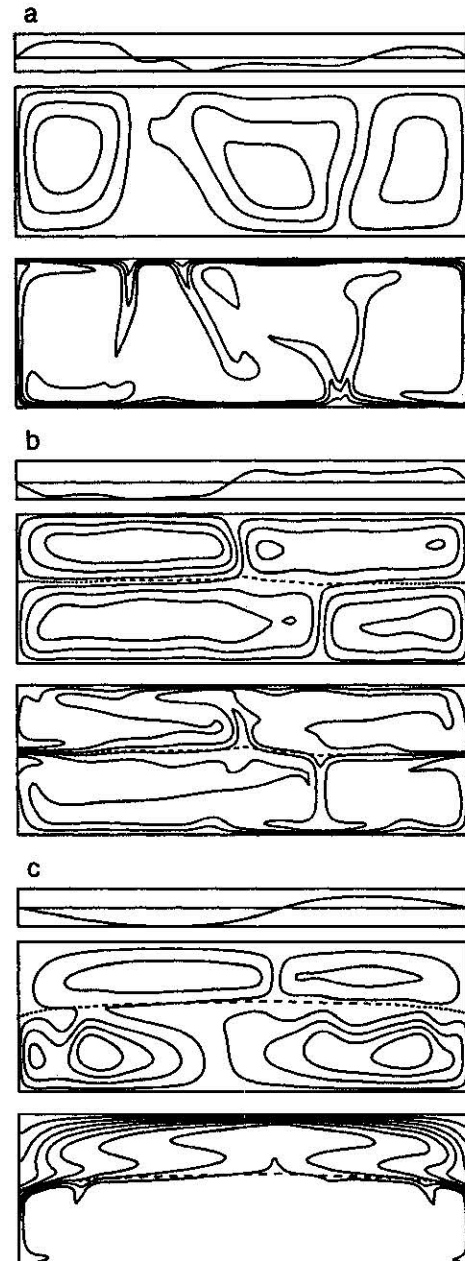


Figure 4. Representative temperature and stream functions for (a) isoviscous flow with no phase change (case 9), (b) isoviscous flow with an endothermic phase change (case 10), and (c) a temperature-dependent viscosity case with an endothermic phase change (case 30). The dashed lines represent the endothermic phase change boundary. For other details, see Figure 3. Note that six contours are used in Figures 4a and 4b, but eight contours are used in Figure 4c in order to visualize the weak thermal wisps in the lower layer.

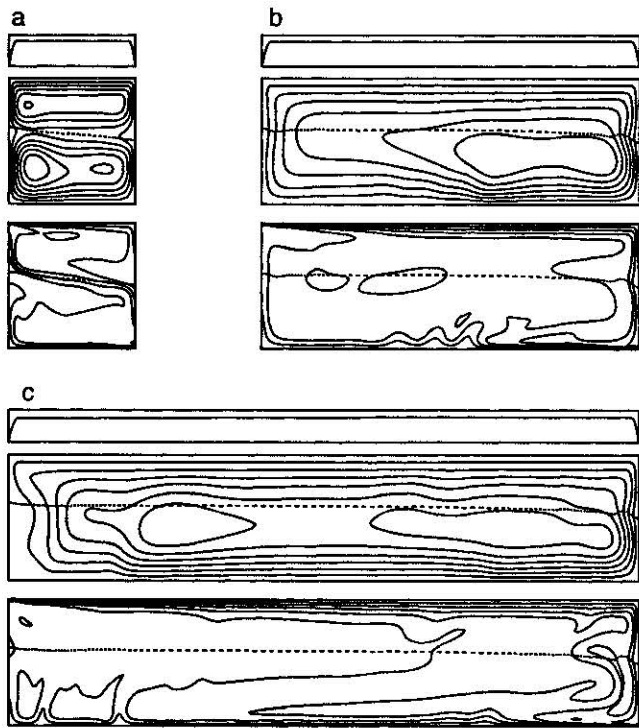


Figure 5. Representative temperature and stream functions for cases with an endothermic phase change and a plate of different length: (a) case 11 with $L = 1$, (b) case 13 with $L = 3$, and (c) case 14 with $L = 5$. For other details, see Figure 4.

degree of layered convection and intermittent slab penetration.

Increasing slab penetration and mass exchange across the phase boundary with L is also evident through the time averaged quantities, $\langle M_v \rangle$ and $\langle V_s \rangle$. Both $\langle M_v \rangle$ and $\langle V_s \rangle$ increase rapidly with L at a rate much larger than that for cases without a phase change (cases 1 - 4 in Table 2). As L increases, both $\langle M_v \rangle$ and $\langle V_s \rangle$ approach $\langle M_h \rangle$ and $\langle U_p \rangle$, respectively (Table 2 and Figures 7a and 7b). For $L = 1$ (case 11), $\langle V_s \rangle$ is only about one third of $\langle U_p \rangle$, and the ratio of $\langle M_v \rangle$ to $\langle M_h \rangle$ is 0.16 (Table 2 and Figure 7b). For $L = 5$ (case 14), $\langle V_s \rangle$ is 0.96 of $\langle U_p \rangle$, and the ratio of $\langle M_v \rangle$ to $\langle M_h \rangle$ is about 0.99 (Table 2 and Figure 7b), a ratio close to that expected from a dominantly single-cell convection with no phase change (e.g., case 4). A predominantly layered system of convection when $L = 1$ (case 11) becomes essentially unlayered when L is increased to 5 (case 14), indicating that the ability of the phase change to affect the style of convection diminishes as plate size increases.

For large L , slab penetration is influenced by an endothermic phase change, and V_s is often much smaller than U_p . V_s always has a very large fluctuation, independent of plate length (Figures 6b and 6c); the standard deviations of V_s are always comparable to $\langle V_s \rangle$ and increase as $\langle V_s \rangle$ increases (values in parentheses in Table 2). Nevertheless, the effects of plate length L on slab penetration are evident not only through the increase of $\langle V_s \rangle$ with L but also through the increase of the time when V_s is larger than $0.80U_p$ normalized by total time R_s (Table 2 and Figures 7a and 7b). R_s increases from 0.05 when $L = 1$ to 0.48 when $L = 5$ (Table 2 and Figure 7b), indicating that slab penetration occurs more frequently for a long plate compared to a short plate.

M_v , M_h , and U_p have smaller fluctuations as L increases (Table 2 and Figures 6b and 6c); for L greater than 2, the standard deviations of M_v , M_h , and U_p decrease as $\langle M_v \rangle$, $\langle M_h \rangle$, and $\langle U_p \rangle$ increase (Table 2). This is significantly different from the large fluctuations which are always observed for V_s . This suggests that the phase change may have less effects on M_v , M_h , and U_p than on V_s , especially when L is large. Moreover, while V_s , M_v , M_h , and U_p usually simultaneously reach maxima and minima in their values, V_s may occasionally be out of phase with M_v , M_h , and U_p for $L = 3$ and 5 (Figures 6b and 6c). This could be due to M_v , M_h , and U_p being controlled by different scale structure than V_s . While only plate-scale structures are capable of affecting M_v , M_h , and U_p , small-scale structures can influence V_s . For a larger L , the phase change has less effect on plate-scale structures, as discussed before; therefore M_v , M_h , and U_p have smaller fluctuations which are presumably caused by the phase change. This explanation is supported by the correlations between plate-scale features including M_v , M_h ,

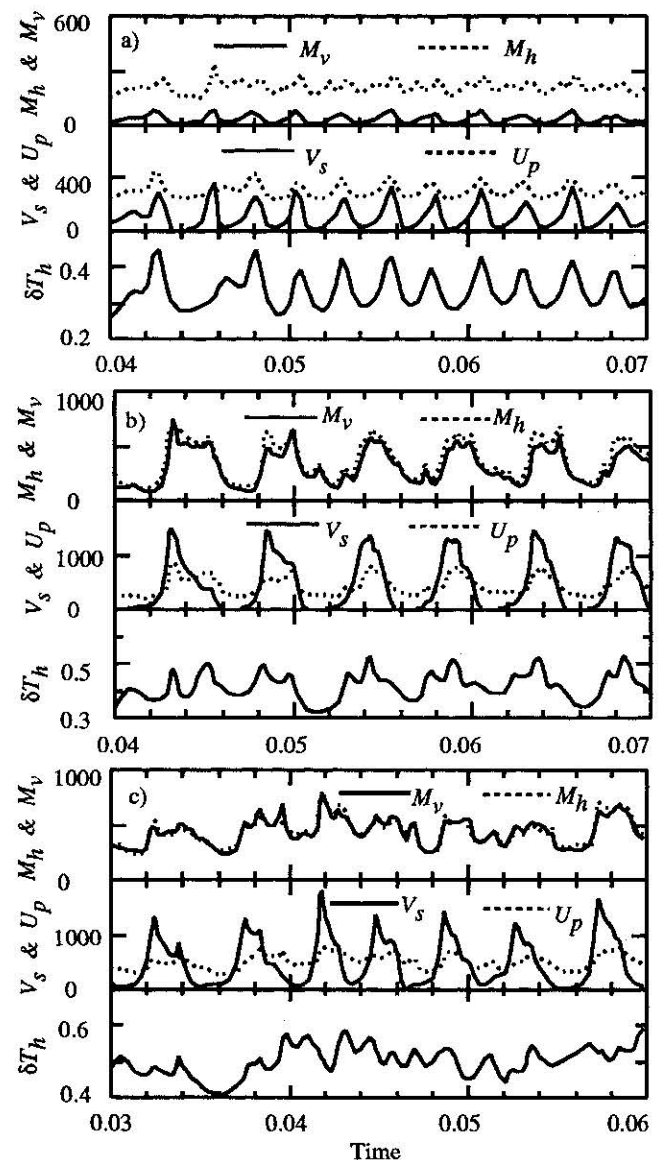


Figure 6. Time history of M_v , M_h , V_s , U_p , and δT_h for (a) case 11, (b) case 13, and (c) case 14. The symbols are defined in the text.

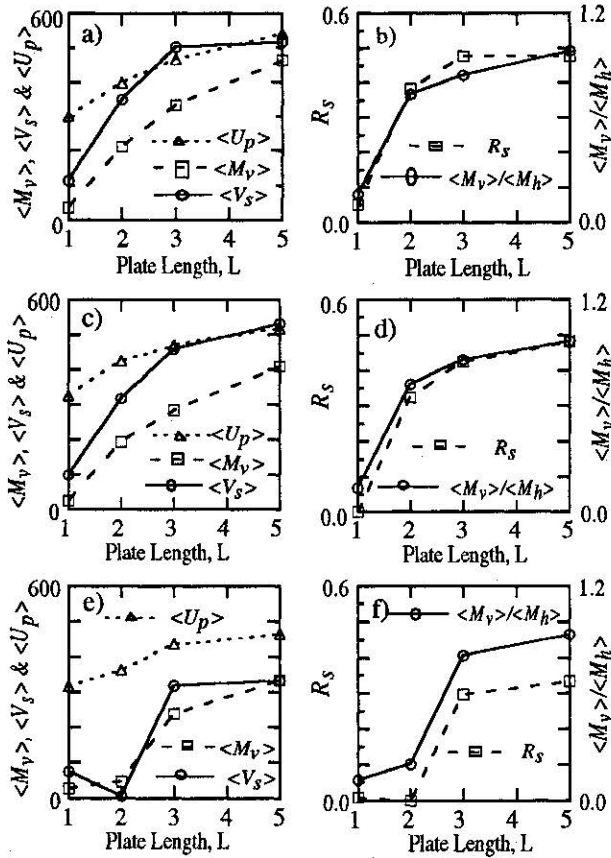


Figure 7. $\langle M_v \rangle$, $\langle V_s \rangle$, $\langle U_p \rangle$, the ratio of $\langle M_v \rangle$ to $\langle M_h \rangle$, and R_s , versus plate length for cases 11-14 (Figures 7a and 7b), cases 15-18 (Figures 7c and 7d), and cases 19-22 (Figures 7e and 7f).

U_p , and δT_h , which measures the largest-scale thermal anomalies (Figures 6a, 6b, and 6c). While δT_h is usually correlated with M_v , M_h , and U_p , independent of L , δT_h only has a correlation with V_s for small L (Figures 6a, 6b, and 6c). Like $\langle U_p \rangle$, $\langle M_v \rangle$, and $\langle M_h \rangle$, time-averaged δT_h , $\langle \delta T_h \rangle$, increases with L (Table 2 and Figure 7b).

When a significant amount of internal heating is included (cases 15, 16, 17, and 18 for $L=1, 2, 3$, and 5, respectively), similar results are obtained. Four internally heated cases are identical to four bottom-heated cases except that the internal heating parameter E is 8 (Table 2). For $L=1$ (case 15), M_v and V_s are much smaller than M_h and U_p , respectively (Figure 8a), like the bottom heated case with $L=1$ (Figure 6a for case 11), indicating layered convection. A steady state is now reached (Figure 8a), while convection is episodic for the bottom-heated case (Figure 6a for case 11). As L becomes larger than 1, convection becomes episodic; V_s occasionally is much larger than U_p ; M_v increases and approaches M_h (Figures 8b and 8c for cases 16 and 17 with $L=2$ and 3, respectively). For $L=3$, M_v essentially overlaps with M_h (Figure 8c), indicating insignificant layering for $L=3$. δT_h correlates with M_v , M_h and U_p (Figures 8b and 8c), but some secondary peaks in δT_h often do not correlate with V_s for large L (Figure 8c). $\langle M_v \rangle$, $\langle V_s \rangle$, $\langle U_p \rangle$ and R_s also increase substantially with L (Figures 7c and 7d and Table 2). Compared with those models with no internal heating, $\langle M_v \rangle$ decreases slightly and there is no significant change in $\langle V_s \rangle$ and $\langle U_p \rangle$ (Table 2 and Figures 7a and 7c), suggesting a minor effect of

internal heating on mass exchange and slab penetration across the phase change boundary, but heat flux F and mean temperature T_m due to the significant internal heating, both increase (Table 2). The internal heating rates, ξ , found a postpriori (Table 2), are 55%, 42%, 41%, and 43% for $L=1, 2, 3$, and 5, respectively (cases 15, 16, 17, and 18).

Although an endothermic phase change has a diminishing effect on mass exchange across the phase boundary as L increases, the phase change still causes slabs to bend and retards penetration even when $L=3$ and 5 (Figures 6b, 6c, and 8c for cases 13, 14, and 17, respectively). A sequence of snapshots of temperature and flow fields for the internally heated case with $L=3$ (case 17) illustrate this process. At time A (time markings in Fig 8c), M_v , V_s , and U_p peak (Figure 8c); cold material within the downwelling penetrates the phase change (Figure 9a), accompanying a high horizontal thermal anomaly δT_h (Figure 8c). The slab penetration results in a low

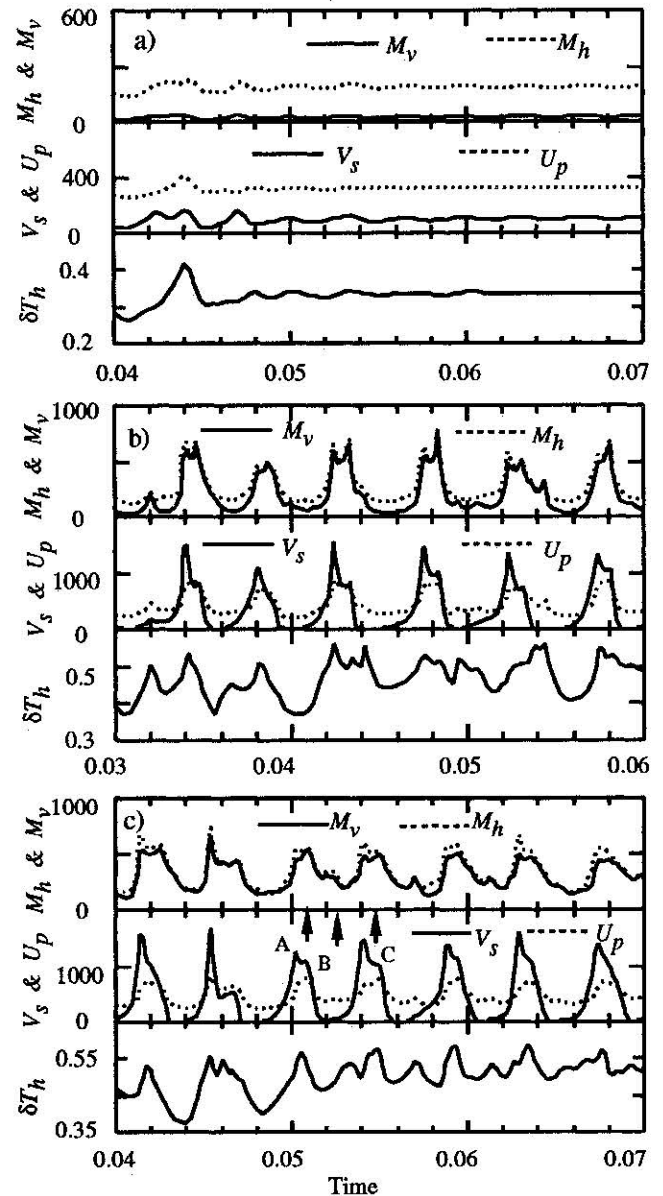


Figure 8. Time history of M_v , M_h , V_s , U_p , and δT_h for cases with an endothermic phase change, internal heating, and a plate of different length: (a) case 15 with $L=1$, (b) case 16 with $L=2$, and (c) case 17 with $L=3$.

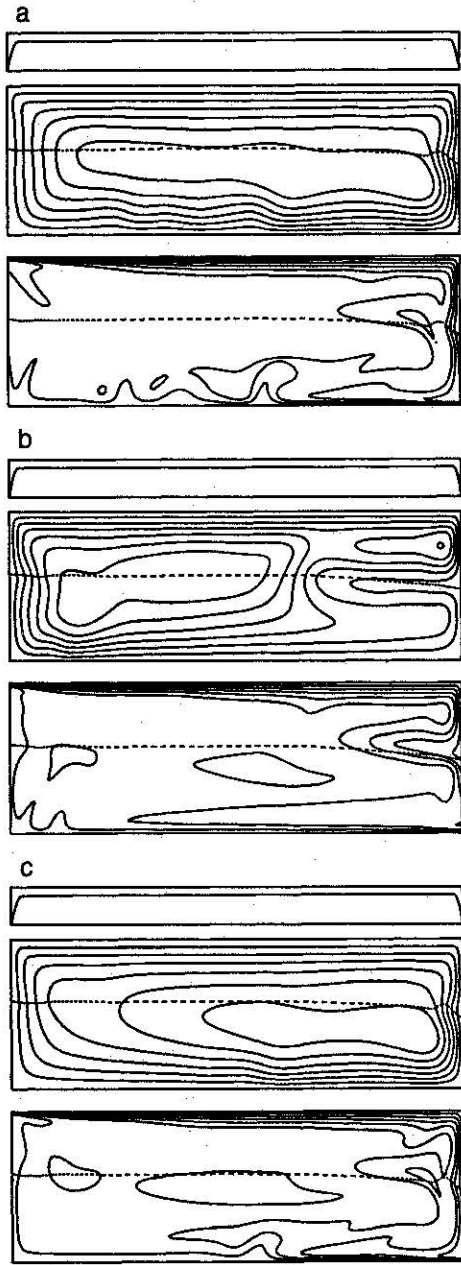


Figure 9. Temperature and stream functions at three instants in time, (a) A, (b) B, and, (c) C for case 17 (see the time markings in Figure 8c); for other details, see Figure 4.

temperature within the slab at the phase boundary with a large deflection of the boundary (Figure 9a), which gives rise to large phase change buoyancy. The increasing phase change buoyancy eventually causes the downwelling slab to bend and cold material to pile up above the phase change boundary by time B (Figures 8c and 9b). At time B, slab penetration velocity V_s is at a minimum along with M_v and U_p (Figure 8c); δT_h is also at a minimum, indicating a small horizontal thermal anomaly (Figure 8c). U_p is now significantly larger than V_s , so cold material tends to pile up above the phase boundary. As the slab bends horizontally, thermal buoyancy accumulates above the phase change boundary and phase change buoyancy decays because the higher temperature at the phase change gives less deflection of the phase boundary (Figure 9b). As the thermal buoyancy dominates at time C, the

downwelling slab penetrates again (Figure 9c), and M_v , V_s , and U_p all reach their maximums (Figure 8c). The horizontal thermal anomaly δT_h also peaks. Even when slab penetration stops (Figure 9b), plate-scale flow structures still dominate, and there is significant mass exchange across the phase change boundary (Figure 8c).

A steeper Clapeyron slope gives rise to larger deflections of phase boundaries, i.e., more phase change buoyancy; hence there is more resistance to slab penetration and mass exchange across the phase boundary. The effects of Clapeyron slope on thermal convection with plates are investigated in four cases with different plate lengths (cases 19, 20, 21, and 22 for $L = 1, 2, 3$, and 5, respectively), and these four cases only differ from the previous internally heated cases (cases 15, 16, 17, and 18) by an increased Clapeyron slope, $\gamma = -0.19$ (Table 2). The effects of plate length on phase change dynamics and flow structures for $\gamma = -0.19$ are similar to those for smaller γ . Convection remains episodic (Figures 10a, 10b, and 10c are time history plots for cases 20, 21, and 22, with $L = 2, 3$, and 5, respectively). As plate length L increases, $\langle M_v \rangle$ and $\langle V_s \rangle$ increase and become as large as $\langle M_h \rangle$ and $\langle U_p \rangle$, respectively (Table 2 and Figure 7e). R_s also increases with L (Table 2 and Figure 7f), but slab penetration is occasionally interrupted by the phase change for large L (Figures 10b and 10c for $L = 3$ and 5). Predominant flow structures are of plate-scale wavelength (Figure 11a for representative temperature and stream functions for case 22 with $L = 5$).

Compared with $\gamma = -0.17$ (cases 15-18), the steeper γ results in more sluggish convection and a less efficient heat transfer. R_s , $\langle U_p \rangle$, $\langle V_s \rangle$, $\langle M_v \rangle$, and heat flux F all decrease (Table 2 and Figures 7c, 7d, 7e and 7f); none of these trends are surprising in light of past analysis [Christensen and Yuen, 1985]. Convection is layered not only for the case (case 19) with $L = 1$ but also for $L = 2$ (case 20) (Table 2 and Figures 10a, 7f, 11b). Layering vanishes for $L = 3$ (Figure 10b for case 21) and the ratio of $\langle M_v \rangle$ to $\langle M_h \rangle$ increases rapidly to 0.81 (Figure 7f and Table 2), which is only slightly smaller than that when $\gamma = -0.17$ for the same plate length (case 17 in Table 2 and Figure 7d). Convection for $L = 2$ (Figure 11b) is characterized by "leaking" convection, as originally discovered by Christensen and Yuen [1985]; this is different from complete layering as seen for $L = 1$ (e.g., Figure 5a). It should be pointed out that $\langle V_s \rangle$ for $L = 2$ is smaller than that for $L = 1$ even though the degree of layering as measured by the ratio of M_v to M_h is less for $L = 2$ than for $L = 1$ (Table 2 and Figures 7e and 7f). This is because an upwelling limb has developed under the downwelling limb and prevents the downwelling limb from penetration (Figures 10a and 11b). The unstable balance between the upwelling and downwelling limbs is maintained by the fixed vertical boundary where flow cannot move horizontally due to the reflecting boundary conditions; clearly, this is a model limitation and is probably irrelevant for Earth's mantle.

In order to further examine the effects of Clapeyron slope, three other cases for $L = 3$ with different γ (γ are -0.12 , -0.15 and -0.21 for cases 23, 24, and 25, respectively; see Table 2) were computed. Together with cases 17 and 21 in which γ are -0.17 and -0.19 , respectively, we see that a steeper γ results in a more sluggish convection, evident through a smaller $\langle M_v \rangle$, $\langle V_s \rangle$, and $\langle U_p \rangle$ (Table 2 and Figure 12a), and a larger degree of layered convection, evident through a smaller ratio of $\langle M_v \rangle$ to $\langle M_h \rangle$ and R_s (Table 2 and Figure 12b). For $\gamma = -0.12$ (case 23), the ratio of $\langle M_v \rangle$ to $\langle M_h \rangle$ and R_s (Table 2

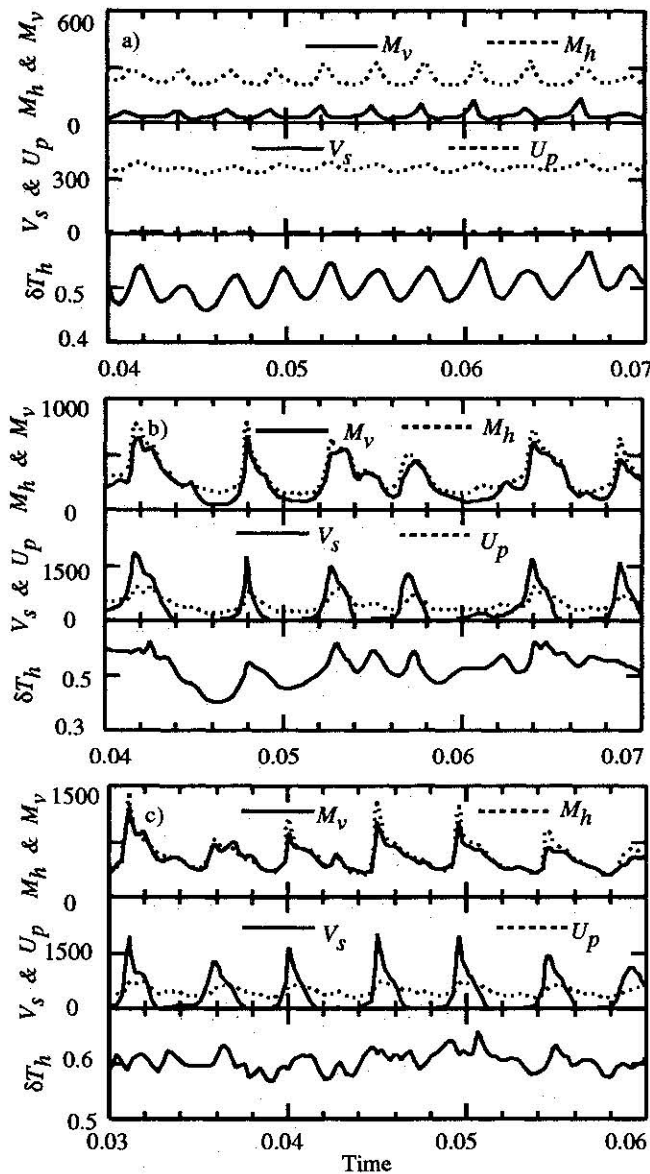


Figure 10. Time history of M_v , M_h , V_s , U_p , and δT_h for cases with an increased strength of endothermic phase change and a plate of different length: (a) case 20 with $L = 2$, (b) case 21 with $L = 3$, and (c) case 22 with $L = 5$.

and Figure 12b) indicate that the phase change is too weak to affect mass exchange across the phase change; the standard deviations of M_v , V_s , and U_p are also relatively small compared with their time averages (Table 2 and Figure 12b), indicating a weak episodicity in thermal convection. For $\gamma = -0.21$ (case 25), the ratio of $\langle M_v \rangle$ to $\langle M_h \rangle$ drops to 0.36 from 0.81 for the case with $\gamma = -0.19$ (case 21) (Figure 12b and Table 2), indicating significant layered convection. This ratio of $\langle M_v \rangle$ to $\langle M_h \rangle$ for $\gamma = -0.21$ is only slightly larger than the 0.33 for the isoviscous case with $\gamma = -0.17$ (case 10 in Table 2), indicating an important effect of γ on the style of convection. V_s and R_s become negligibly small for $\gamma = -0.21$ (Figure 13a for time history, Figure 12b and Table 2). The insignificant slab penetration is due to the formation of an upwelling limb in the lower layer beneath the downwelling within the upper layer (Figure 11c for representative temperature and stream functions), similar to that observed for

the case with $\gamma = -0.19$ and $L = 2$ (Table 2, Figures 10a and 11b). Interestingly, for $\gamma = -0.21$, the episodicity in thermal convection is also relatively weak, compared with those for small γ , except for $\gamma = -0.12$ (Figures 8c, 10b, and 13a for cases with $\gamma = -0.17$, -0.19 , and -0.21 , respectively), which is also evident through the ratios of standard deviations of M_v , V_s and U_p to their time averages (Figure 12b and Table 2). This suggests that a strong episodic convection induced by the phase change only occurs within a certain range of Clapeyron slopes.

The effects of plates when an additional exothermic phase change at 410 km depth is present are investigated with four cases of different plate length (cases 26, 27, 28, and 29 for $L = 1, 2, 3$, and 5, respectively; see Table 2). In these four cases, the exothermic phase changes have the same strength as the endothermic phase change ($R_b^1 = R_b^2 = 2 \times 10^6$, $\gamma_1 = 0.17$, and $\gamma_2 = -0.17$). An exothermic phase change tends to counteract the effect of an endothermic phase change and enhances thermal convection [Schubert et al., 1975; Christensen and Yuen, 1985].

The results from these internally heated cases with two phase changes are similar to the results when only one endothermic phase change is present. A substantial increase in

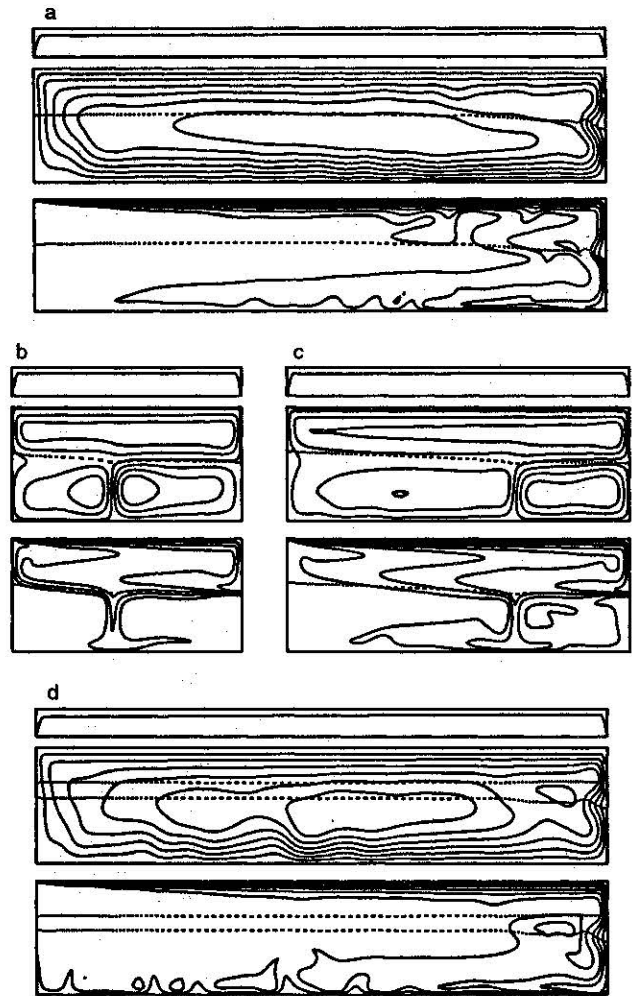


Figure 11. Representative temperature and stream functions for cases (a) 22, (b) 20, (c) 25, and (d) 29, respectively. An exothermic phase change is included in case 29, and the exothermic phase change boundary is indicated by the upper dashed line (Figure 11d). For other details, see Figure 4.

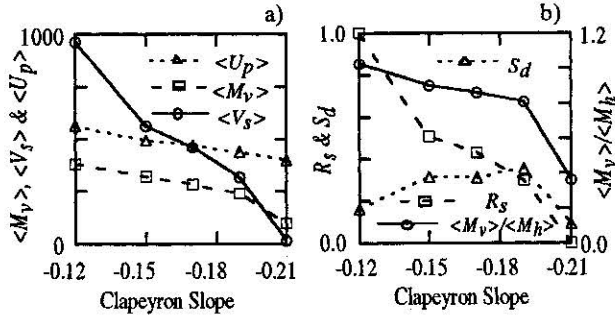


Figure 12. (a) $\langle M_v \rangle$, $\langle V_s \rangle$, $\langle U_p \rangle$, (b) the ratio of $\langle M_v \rangle$ to $\langle M_h \rangle$, R_s , and the ratio of the standard deviations of U_p to $\langle U_p \rangle$ (i.e., S_d) versus Clapeyron slope for cases 17, 21, 23, 24 and 25.

the mass exchange and slab penetration across the endothermic phase boundary, as plate length L increases, is observed (R_s , $\langle M_v \rangle$, and $\langle V_s \rangle$ in Table 2). As L increases, the ratio of $\langle M_v \rangle$ to $\langle M_h \rangle$ increases (Table 2), indicating a diminished effect of the endothermic phase change on mass exchange across the phase change for a larger L . Plate-scale flow structures always predominate (Figure 11d for case 29). Inclusion of the exothermic phase change results in more vigorous convection and more efficient heat transfer, compared to those cases with only an endothermic phase change (e.g., cases 15-18), evident from the increases in $\langle M_v \rangle$, $\langle V_s \rangle$, $\langle U_p \rangle$, $\langle \delta T_h \rangle$, R_s and F (Table 2).

It is important to realize that the material property method always yields a "plate-like" surface velocity with a plateness close to 0.9 for models with different plate lengths, different phase change parameters, and different heating modes (Table 2 and Figures 5, 9, and 11). The continuous cooling of the top thermal boundary layer is well simulated (Figures 5, 9, and 11), although minor boundary layer instabilities start to develop close to the major downwellings for $L = 5$ (e.g., Figures 5c and 11a). The plate velocity U_p and the mass flux M_v are often both correlated with δT_h (see all the history plots). $\langle U_p \rangle$ increases with plate length L (Table 2), as expected from the increase of $\langle \delta T_h \rangle$ with L (Table 2). Plate motion is controlled by plate-scale structures which are generated due to the presence of plates. This is similar to the results reported by Zhong and Gurnis [1993].

Effects of Stiff Slabs

We have shown that stiff plates have important effects on phase change dynamics. Stiff plates result from temperature-dependent rheology of the Earth's mantle, and the same rheology will make subducted slabs stiff. Because a stiff subducted slab will tend to retain its shape, slab strength may have important effects on phase change dynamics, including slab penetration [Christensen and Yuen, 1984]. In this section, we shall use temperature-dependent rheology to investigate the effects of stiff slabs, which were not addressed in our previous material property plate models.

For proper comparisons between different cases, it is essential to have the same thermal Rayleigh number, since effects of phase changes on mass exchange across endothermic phase change depend on the Rayleigh number [Christensen and Yuen, 1985; Zhao et al., 1992]. R_a was 10^6 for previous cases with dynamic plates; for temperature-dependent viscosity cases, R_a defined with the viscosity at

the bottom boundary temperature is chosen such that the R_a defined with the averaged viscosity over the domain excluding the region for the high-viscosity lids is approximately 10^6 .

While temperature-dependent viscosity makes both plates and subducted slabs stiff, the resulting surface velocity does not resemble "plate-like" velocity [e.g., Gurnis, 1989]; the magnitude of surface velocity is negligibly small, and there is significant interior strain. This is illustrated by a case with temperature-dependent viscosity, TDV1 (Figure 2), and a free slip boundary condition (case 30 in Table 2; see Figure 4c for representative temperature and flow fields and surface velocity). The upper layer due to its relatively low temperature is much less mobile than the lower layer (Figure 4c), and the average surface velocity is 74 (Table 2), significantly smaller than the bottom average velocity of 300 and also much smaller than the average surface velocity for the isoviscous flow model (case 10 in Table 2) which only differs from this temperature-dependent viscosity case (case 30) in rheology. Moreover, there is significant interior strain in surface velocity (Figure 4c). Compared with the isoviscous case (case 10), the degree of layering as measured by the ratio of $\langle M_v \rangle$ to $\langle M_h \rangle$ only changes slightly (Table 2); the immobile top boundary results in a substantial decrease in surface heat flux F (Table 2). The significantly high internal heating rate for case 30 is due to the relatively uniform temperature in the lower layer (Figure 4c), which stifles the flow of heat into the bottom boundary.

In order to obtain a realistic plate in temperature-dependent viscosity models, a plate generation method is necessary. Following Davies [1988a], a constant velocity is imposed on

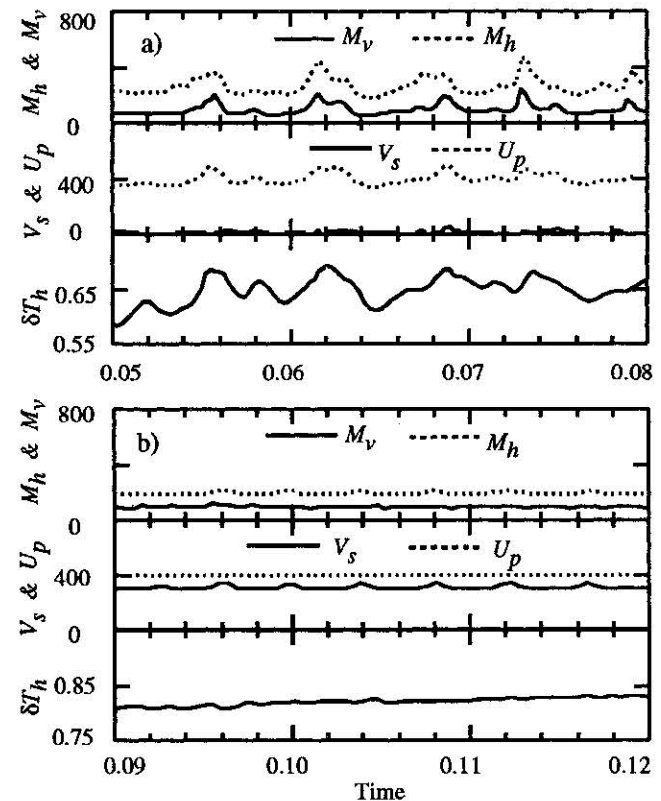


Figure 13. Time history of M_v , M_h , V_s , U_p , and δT_h for cases with $\gamma = -0.21$ but with different rheology: (a) case 25 with the material property method and (b) case 35 with a temperature-dependent viscosity, TDV1.

the surface as a boundary condition. The surface velocity has to be chosen properly such that on average over a long period of time no significant amount of extra kinetic energy is introduced into the system. Before introducing the imposed surface velocity plate into temperature-dependent viscosity models, we will first demonstrate that if the averaged plate velocity from a material property model is taken as the imposed velocity for a model with a same Rayleigh number and Clapeyron slope, the imposing surface velocity does not significantly alter the dynamics of the system.

Two cases (cases 31 and 32 in Table 2) with imposed constant surface velocities on high-viscosity lids without weak margins are computed. The imposed surface velocities for cases 31 and 32 are the averaged plate velocities for cases 7 and 17 (Table 2), respectively; the latter two cases with dynamic plates differ from the former two only in having two weak margins and a free-slip top surface. Both the time-averaged quantities including $\langle M_v \rangle$, $\langle M_h \rangle$, $\langle V_s \rangle$, R_s , F , ξ , and T_m and their time dependencies for these two imposed surface velocity cases (cases 31 and 32) are nearly identical to those for models with dynamic plates (cases 7 and 17) (Table 2 and Figures 8c and 14a for time dependence for cases 17 and 32, respectively).

Given the above justifications of using imposed surface velocity, we then introduce temperature-dependent rheology along with the imposed surface velocity into three cases (cases 33-35). Cases 33, 34, and 35 with temperature-dependent rheology differ from previous cases 7, 17, and 25 (Table 2), respectively, in only the rheology and surface boundary conditions; the imposed surface velocities for these temperature-dependent viscosity cases are the averaged plate velocities for previous cases with dynamic plates (Table 2). The temperature dependence of viscosity for these three cases (cases 33-35) is the TDV1 (Figure 2). M_v and V_s for the temperature-dependent viscosity case with no phase change (case 33) decrease, but heat flux F increases, compared to those for the case with material property plates (case 7) (Table 2). The higher viscosity of slabs tends to decrease V_s and makes V_s closer to the plate velocity (Table 2).

For the cases with the phase change, temperature-dependent viscosity results in significant changes in slab penetration and the episodicity of convection, compared with cases with only stiff plates (see time dependence, Figures 8c and 14b for cases 17 and 34, respectively, with $\gamma = -0.17$; Figures 13a and 13b for cases 25 and 35, respectively, with $\gamma = -0.21$). For case 34, $R_s = 1.0$; V_s is always close to U_p with insignificant episodicity (Table 2 and Figure 14b), indicating that the downwelling continuously penetrates the phase boundary (Figure 15a for representative temperature and flow fields). This is significantly different from case 17 with only stiff plates, in which case, slab penetration is frequently stopped by the phase change with a strong episodicity (Figures 8c and 9). More dramatic changes resulting from stiff slabs in slab penetration occur when $\gamma = -0.21$ (cases 25 and 35). In case 25 with no stiff slab, slabs cannot penetrate through the phase change (Figure 11c for temperature and flow fields and Figure 13a for time dependence), but slabs penetrate steadily through the phase change when slabs are made stiff through temperature-dependent viscosity in case 35 (Figure 13b for time dependence and Figure 15b for representative temperature and flow fields). R_s is 0.26 for case 35 (Table 2). This is due to the definition of R_s , in which the occurrence of penetration is when V_s is larger than 0.8 of U_p ; indeed, V_s is always about

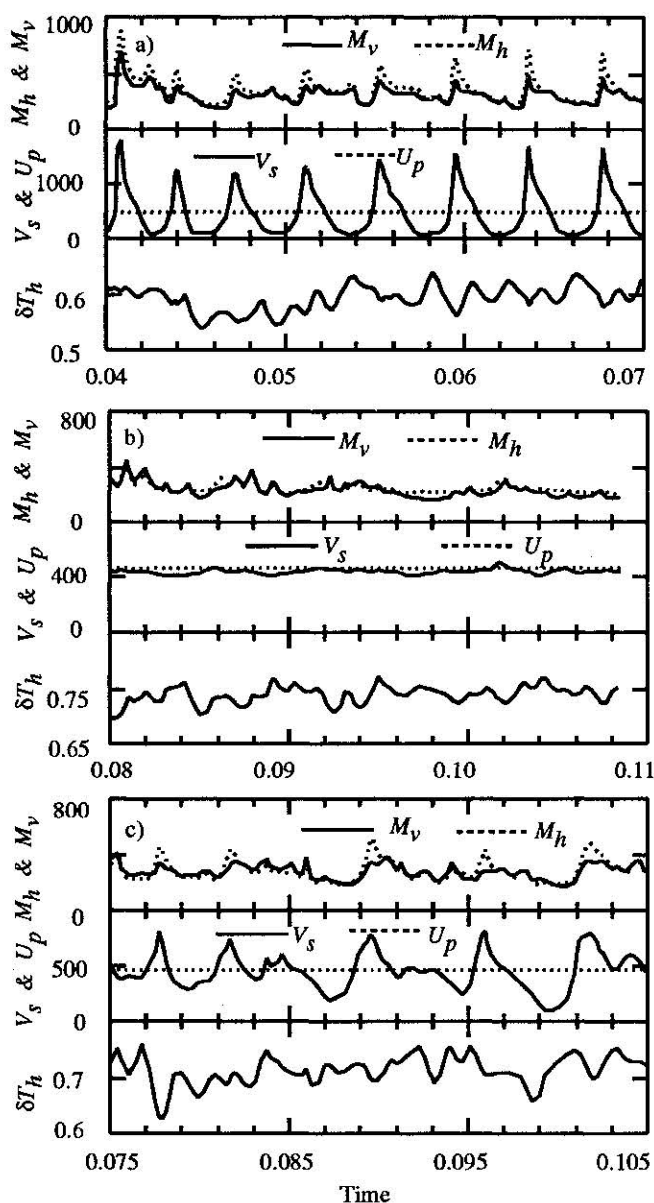


Figure 14. Time history of M_v , M_h , V_s , U_p , and δT_h for cases with $\gamma = -0.17$ but with different rheology: (a) case 32 with a high viscosity plate of imposed surface velocity, (b) case 34 with TDV1, and (c) case 36 with TDV2.

0.75 of U_p (Figure 13b). The episodicity in thermal convection is substantially diminished for this temperature-dependent viscosity case (case 35), compared to the case with no stiff slabs (case 25). Interestingly, the temperature-dependent rheology only slightly reduces the degree of layering, as indicated by the ratios of $\langle M_v \rangle$ to $\langle M_h \rangle$ (Table 2). For case 35, even though slabs steadily penetrate through the phase change due to temperature-dependent viscosity, convection is still significantly layered, evident through the ratio of $\langle M_v \rangle$ to $\langle M_h \rangle$, which is 0.47 (Table 2), the time dependence of M_v and M_h (Figure 13b), and the representative flow field (Figure 15b).

Comparison between the temperature-dependent viscosity cases with a plate (case 34) and that with no plate (case 30) reveals the effects of a plate. Case 34 differs from case 30 only in having a mobile plate by imposing surface velocity. The

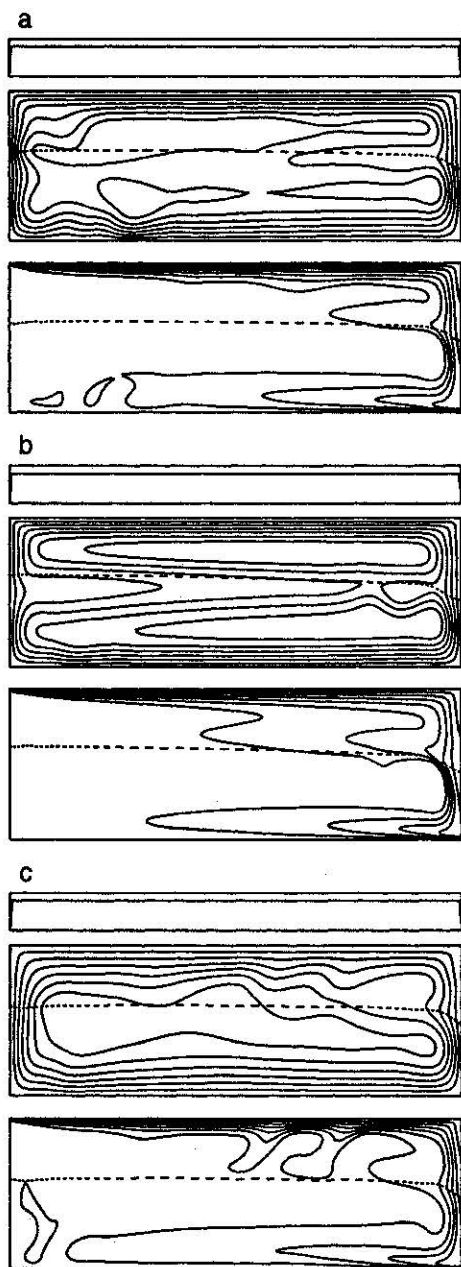


Figure 15. Representative temperature and stream functions for temperature-dependent viscosity cases: (a) case 34, (b) case 35, and (c) case 36, respectively. For other details, see Figure 4.

ratio of $\langle M_v \rangle$ to $\langle M_h \rangle$ is 0.93 for case 34 but is only 0.28 for case 30 (Table 2), indicating that the presence of plates significantly reduces the degree of layering, which is also evident in the flow fields (Figures 4c and 15a). Together with the observation that rheology can significantly change slab penetration but has little effects on the degree of layering for a given plate length (e.g., cases 25 and 36 for $\gamma = -0.21$ in Table 2), this again suggests that global features including mass flux and the degree of layering are controlled by large-scale structures organized by plates, while slab penetration is more related to local features.

Temperature-dependent viscosity gives rise to high strength slabs; slabs with high strength tend to retain their integrity and thus enhance slab penetration. Slab penetration

depends on the strength of slabs. The effect of a different temperature-dependence of viscosity is examined in case 36 which only differ from case 34 by using a different temperature dependence of viscosity, TDV2 (Figure 2). Since TDV2 gives rise to slabs which are weaker than those from TDV1 (case 34) but stronger than those of constant background viscosity (case 17), the results from the case with TDV2 (case 36) are between those from the case with TDV1 (case 34) and those from the case with no stiff slabs (case 17). Thermal convection becomes more episodic, compared to the case with TDV1 (case 34); slab penetration velocity V_s significantly fluctuates, although the fluctuation is smaller than that for the case with no stiff slabs (case 17) (Figure 14c is time dependence for case 36 with TDV2). It should be pointed out that significant thermal boundary layer instabilities occur for the case with TDV2 (case 36) (Figure 15c for representative temperature and flow fields), which may result in leakage in negative buoyancy within plates and thus weakens slab penetration.

Conclusions

Our thermal convection models with multiple phase changes and realistic plates and slabs have consistently shown for different Clapeyron slopes and different heating modes that plates and stiff slabs have a profound effect on phase change dynamics. As plate length increases, slab penetration occurs more frequently; convection becomes less layered; mass flux across endothermic phase change increases. A stiff slab due to temperature-dependent rheology enhances slab penetration but has little effect on total mass flux and degree of layering. These results are of particular importance to the dynamics of western Pacific subduction zones where plate sizes are large.

Plates always generate predominant plate-scale thermal and flow structures, independent of plate length. Plate-scale structures have important controls over the style of convection. As plates become larger, the resulting larger scale structures are less influenced by endothermic phase changes, thus reducing the degree of layering. Our models show that complete layered convection occurring for a plate length equal to the thickness of the box becomes insignificantly layered as the plate length increases to 3 or 5 times larger and that the time ratio of slab penetration can increase from zero for cases with small plates to more than 0.5 for cases with large plates.

We suggest that large-scale features including degree of layering, plate velocity, and mass flux are controlled by large-scale structures, while slab penetration may be related more to small-scale features. Therefore, whether or not subducted slabs penetrate the phase change may not necessarily indicate that convection is layered or unlayered. Unlayered convection can coexist with no slab penetration (e.g., Figure 6c for case 14) and steady slab penetration can coexist with significantly layered convection (e.g., Figures 13b and 15b for case 35).

The episodicity of convection induced by the endothermic phase changes strongly depends on plate length, rheology, and Clapeyron slope. As long as plate size increases to a certain length, further increases in plate length would weaken the episodicity of convection (e.g. Figures 6, 8 and 10). When slabs become stiff with temperature-dependent rheology, episodicity in convection also weakens substantially (e.g., Figure 13a versus Figure 13b and Figure 8c versus Figure 14b). Only for a certain range of Clapeyron slope, can the phase

change induce a strong episodic thermal convection; any endothermic phase change with Clapeyron slope larger or smaller than this range tends to give a more steady convection (Figure 12b).

The proper simulations of plates and subducted slabs are essential for mantle convection models. The material property method, because it effectively takes into account both temperature- and stress- dependent rheology, provides a very successful tool to simulate plates even for a plate as long as 5 times the thickness of the fluid layer. Imposed surface velocity together with temperature-dependent viscosity can simulate both plates and stiff slabs, although it is computationally costly.

Acknowledgment. We appreciate the discussions with S. Weinstein and reviews by S. King, G. Davies, and an anonymous reviewer. Many of the computations were carried at the Pittsburgh Supercomputer Center. Funded by the David and Lucile Packard Foundation and NSF grant EAR-8957164.

References

- Brooks, A. N., A Petrov-Galerkin finite element formulation for convection dominated flows, Ph.D. thesis, Calif. Inst. of Technol., Pasadena, 1981.
- Cazenave, A., and B. Lago, Long wavelength topography, seafloor subsidence and flattening, *Geophys. Res. Lett.*, **18**, 1257-1260, 1991.
- Christensen, U. R., and D. A. Yuen, Layered convection induced by phase transitions, *J. Geophys. Res.*, **90**, 10,291-10,300, 1985.
- Christensen, U. R., and D. A. Yuen, The interaction of a subducting lithospheric slab with a chemical or phase boundary, *J. Geophys. Res.*, **89**, 4389-4402, 1984.
- Davies, G. F., Role of the lithosphere in mantle convection, *J. Geophys. Res.*, **93**, 10,451-10,466, 1988a.
- Davies, G. F., Ocean bathymetry and mantle convection, 1, Large-scale flow and hotspots, *J. Geophys. Res.*, **93**, 10,467-10,480, 1988b.
- Davies, G. F., Ocean bathymetry and mantle convection, 2, Small-scale flow, *J. Geophys. Res.*, **93**, 10,481-10,488, 1988c.
- Davies, G. F. and F. Pribac, Mesozoic seafloor subsidence and the Darwin Rise, past and present, in *The Mesozoic Pacific: Geology, Tectonics, and Volcanism*, *Geophys. Monogr. Ser.*, vol. 77, edited by M. Pringle, W. Sager, W. Sliter and S. Stein, pp. 39-52, AGU, Washington, D. C., 1993.
- Gable, C. W., R. J. O'Connell, and B. J. Travis, Convection in three dimensions with surface plates: Generation of toroidal flow, *J. Geophys. Res.*, **96**, 8391-8405, 1991.
- Gurnis, M., A reassessment of the heat transport by variable viscosity convection with plates and lids, *Geophys. Res. Lett.*, **16**, 179-182, 1989.
- Gurnis, M., and B. H. Hager, Controls on the structure of subducted slabs, *Nature*, **335**, 317-321, 1988.
- Heestand, R. L., and S. T. Crough, The effect of hotspots on the oceanic age-depth relation, *J. Geophys. Res.*, **86**, 6107-6114, 1981.
- Honda, S., S. Balachandar, D. A. Yuen, and D. Reuteler, Three-dimensional instabilities of mantle convection with multiple phase transitions, *Science*, **259**, 1308-1311, 1993.
- Hughes, T. J. R., *The Finite Element Method*, 631 pp., Prentice-Hall, Englewood Cliffs, N.J., 1987.
- King, S. D., C. W. Gable, and S. A. Weinstein, Models of convection driven tectonic plates: A comparison of methods and results, *Geophys. J. Int.*, **109**, 481-487, 1992.
- King, S. D., and B. H. Hager, The relationship between plate velocity and trench viscosity in newtonian and power-law subduction calculations, *Geophys. Res. Lett.*, **17**, 2409-2412, 1990.
- King, S. D., Raefsky, A. and Hager, B. H., ConMan: Vectorizing a finite element code for incompressible two-dimensional convection in the Earth's mantle, *Phys. Earth Planet. Inter.*, **59**, 195-207, 1990.
- Machetel, P., and P. Weber, Intermittent layered convection in a model with an endothermic phase change at 670 km, *Nature*, **350**, 55-57, 1991.
- McKenzie, D. P., J. M. Roberts, and N. O. Weiss, Convection in the Earth's mantle: Towards a numerical simulation, *J. Fluid Mech.*, **62**, 465-538, 1974.
- Parsons, B., and J. G. Sclater, An analysis of the variation of ocean floor bathymetry and heat flow with age, *J. Geophys. Res.*, **82**, 803-827, 1977.
- Peltier, W. R., and L. P. Solheim, Mantle phase transitions and layered chaotic convection, *Geophys. Res. Lett.*, **19**, 321-324, 1992.
- Richter, F. M., Finite amplitude convection through a phase boundary, *Geophys. J. R. Astron. Soc.*, **35**, 265-276, 1973.
- Schroeder, W., The empirical age-depth relation and depth anomalies in the Pacific Ocean basin, *J. Geophys. Res.*, **89**, 9873-9884, 1984.
- Schubert, G., D. A. Yuen, and D. L. Turcotte, Role of phase transitions in a dynamic mantle, *Geophys. J. R. astr. Soc.*, **42**, 705-735, 1975.
- Su, W.-J., and A. M. Dziewonski, On the scale of mantle heterogeneity, *Phys. Earth Planet. Inter.*, **74**, 29-54, 1992.
- Tackley, P. J., D. J. Stevenson, G. A. Glatzmeir, and G. Schubert, Effects of an endothermic phase transition at 670 km depth on spherical mantle convection, *Nature*, **361**, 137-160, 1993.
- Weinstein, S. A., Catastrophic overturn of the Earth's mantle driven by multiple phase changes and internal heat generation, *Geophys. Res. Lett.*, **20**, 101-104, 1993.
- Weinstein, S. A., and P. L. Olson, Thermal convection with non-Newtonian plates, *Geophys. J. Int.*, **111**, 515-530, 1992.
- Woodward, R. L., and G. Masters, Global upper mantle structure from *ScS-S* differential travel times, *J. Geophys. Res.*, **96**, 6351-6377, 1991.
- Zhang, Y.S., and T. Tanimoto, Global Love wave phase velocity variation and its significance to plate tectonics, *Phys. Earth Planet. Inter.*, **66**, 160-202, 1991.
- Zhao, W., D. A. Yuen, and S. Honda, Multiple phase transitions and the style of mantle convection, *Phys. Earth Planet. Inter.*, **72**, 185-210, 1992.
- Zhong, S., and M. Gurnis, Dynamic feedback between a non-subducting raft and thermal convection, *J. Geophys. Res.*, **98**, 12,219-12,232, 1993.

M. Gurnis, Seismological Laboratory, California Institute of Technology, Pasadena, CA 91125.

S. Zhong, Department of Geological Sciences, University of Michigan, Ann Arbor, MI 48109-1063.

(Received September 1, 1993; revised January 31, 1994; accepted February 18, 1994.)